Sculpting 3D spatial selectivity with pairs of 2D pulses: A comparison of methods

Gil Farkash, Jean-Nicolas Dumez, Lucio Frydman

Sculpting 3D Spatial Selectivity with Pairs of 2D Pulses: A Comparison of Methods

Gil Farkash[1], Jean-Nicolas Dumez[2] and Lucio Frydman[1]*
[1]*Chemical Physics Department, Weizmann Institute of Science, 76100 Rehovot, Israel*
, [2]*Institut de Chimie des Substances Naturelles, CNRS, 91190 Gif-sur-Yvette, France*

Abstract. Enhancing the specificity of the spins' excitation can improve the capabilities of magnetic resonance. Exciting voxels with tailored 3D shapes reduces partial volume effects and enhances contrast, particularly in cases where cubic voxels or other simple geometries do not provide an optimal localization. Spatial excitation profiles of arbitrary shapes can be implemented using so-called multidimensional RF pulses, which are often limited in practice to 2D implementations owing to their sensitivity to field inhomogeneities. Recent work has shown the potential of spatio-temporally encoded (SPEN) pulses towards alleviating these constraints. In particular, 2D pulses operating in a so-called hybrid scheme where the "low-bandwidth" spatial dimension is sculpted by a SPEN strategy while an orthogonal axis is shaped by regular k-space encoding, have been shown resilient to chemical shift and B_0 field inhomogeneities. In this work we explore the use of pairs of 2D pulses, with one of these addressing geometries in the x-y plane and the other in the x-z dimension, to sculpt complex 3D volumes in phantoms and *in vivo*. To overcome limitations caused by the RF discretization demanded by these 2D pulses, a number of "unfolding" techniques yielding images from the centerband RF excitation while deleting sideband contributions –even in cases where center- and side-bands severely overlap– were developed. Thus it was possible to increase the gradient strengths applied along the low bandwidth dimensions, significantly improving the robustness of this kind of 3D sculpting pulses. Comparisons against conventional pulses designed on the basis of pure k-space trajectories, are presented.

Keywords: 3D RF pulses; Spatiotemporal excitation; field inhomogeneities; In Vivo MRS

Running Title: Robust 3D shaping based on spatiotemporal encoding

Abbreviations: EPI, echo-planar imaging; FFT, Fast Fourier transform; MRI, magnetic resonance imaging; MRS, magnetic resonance spectroscopy; MRSI, magnetic resonance spectroscopic imaging; NMR, nuclear magnetic resonance; PE, phase encoding; RF, radio-frequency; RO, readout; ROI, region of interest; SPEN, spatiotemporal encoding.

* Corresponding author. Fax: +972 8 9344123. E-mail address: lucio.frydman@weizmann.ac.il (L. Frydman).

1. Introduction

Achieving accurate excitation selectivity of complex 3D volumes can be an important aid in magnetic resonance spectroscopy (MRS), imaging (MRI) and spectroscopic imaging (MRSI) studies. By improving localization, voxels with arbitrary 3D shapes enable spectral measurements of organs or tissues with higher specificity [1, 2], as well as improved estimations of relaxation rates [3], diffusion coefficients [4] or chemical concentrations [5, 6]. Most localized studies rely on either selective excitation [7] or outer volume suppression [8]. Both radiofrequency (RF) manipulations usually sculpt a single spatial axis at a time, thereby defining relatively simple shapes. More finely-tuned volumes and shapes can be excited by relying on so-called multidimensional RF pulses [9-11]. Initially developed on the basis of single-shot *k*-space scanning ideas associated with Echo Planar Imaging (EPI), such strategies are commonly used for achieving 2D spatial/spatial and 2D spatial/spectral selectivity. Volume selectivity with *k*-based 3D RF pulses has also been reported in *ex*- and *in vivo* studies [12, 13]. These 3D RF pulses, however, are usually long, which makes them highly sensitive to chemical shift offsets and B_0 field inhomogeneities. Parallel transmission techniques that shorten these pulses, are therefore necessary for sculpting even simple 3D shapes [2, 14]. Still, as parallel transmission can be of limited availability or constrained by specific absorption rates (SAR) [15], exciting complex 3D shapes remains an important open challenge in *in vivo* MR.

This work explores a number of strategies to target complex shaped volumes, based on concatenating pairs of 2D RF pulses. Our attention is focused on alternatives to *k*-based methods that use 2D spatiotemporally encoded (SPEN) pulses. SPEN progressively combines the spins' time evolution with their position along a spatial dimension. While initially devised for acquiring multidimensional NMR and MRI data in a single scan [16-21], recent work has shown SPEN's potential for selective 2D excitations. Compared to their *k*-based counterparts 2D SPEN pulses can have, under the right conditions, an enhanced robustness vis-à-vis field heterogeneities and chemical shifts [22]. Besides their use to selectively excite 2D shapes of arbitrary form, such pulses have also been used to impart arbitrary phases that will compensate for 3D inhomogeneities [23, 24].

Multidimensional RF pulses are usually executed as nested loops, where "fast" spatial excitations are looped within a progressive, slower sculpting. This approach is associated with two features that may limit their applicability. One relates to the discreteness of the "slow" axis sculpting: acting somewhat like a DANTE pulse [25, 26], its gapped nature may result in undesired excitation replicates. The other relates

to the duration of this "slow" axis sculpting, which makes it sensitive to chemical shift misregistrations and B_0 inhomogeneity distortions. It was recently shown that, by addressing spins sequentially via the combined action of magnetic field gradients and frequency-swept pulses, SPEN can alleviate both of these constraints [16]. 2D pulses exploit this by performing a SPEN-based sculpting along the "slow" axis, while retaining the regular Fourier encoding –which is less susceptible to distortions due to its higher associated gradients– along the orthogonal direction. Given the good results observed with this approach [22], the question arose whether this robustness could suffice to enable arbitrary 3D excitations. As an initial step in this direction, this study explores the sculpting of 3D shapes by the concatenation of 2D pulses, possessing one spatial axis in common. Our proposals involved pairing either SPEN- or *k*-based 2D pulses, including an excitation/refocusing pair, or two refocusing 2D pulses transmitted after a pulse has excited one or more chemical sites in the sample (Figs. 1a, 1b). As spins outside the arbitrary planar patterns excited/inverted by these pulses can be crushed by appropriate gradients, complex 3D patterns at the intersection of these 2D shapes will be selected. While the 3D selectivity of this scheme for SPEN- and for *k*-based pulses was comparable in simulated scenarios, the SPEN-based design performed consistently better in *ex vivo* and *in vivo* tests and experiments. The reasons for this, as well as further options to improve the robustness and expand the flexibility of this approach, are discussed.

2. Theoretical Background

Before explaining their use in sculpting 3D shapes, it is convenient to briefly review the SPEN-based RF pulses used in our experiments. As the x-axis was chosen to be the "slow" dimension of the 2D pulses (Fig. 1) we shall assume that, following excitation, a frequency-swept refocusing pulse of duration T_{180} is applied in the presence of a gradient $G_{180}\hat{x}$. Spins will then accrue a phase [17]

$$\varphi_{180}(x) = \left(-\frac{(\gamma G_{180})^2}{R_{180}}\right)x^2 + \left(\gamma G_{180}\left(T_{180} + \frac{2(O_{i,180}-\Omega)}{R_{180}}\right)\right)x + \left(\Omega T_{180} - \frac{(O_{i,180}-\Omega)^2}{R_{180}}\right) \qquad (1)$$

where Ω is a site-specific frequency offset associated to chemical shift or field inhomogeneity effects, $O_{i,180}$ is the initial frequency for the RF sweep, R_{180} is the RF sweep rate and x denotes the spin's spatial position, as determined by the swept pulse and by the encoding gradient $G_{180}\hat{x}$. 2D SPEN-based pulses harness this point-by-point manipulation by breaking it into a train of discrete gradient blips, and

inserting in-between these blips RF pulses acting while activating a second, orthogonal *y*-axis gradient. The shape of these pulses is then tailored so as to perform a selective spins' excitation/inversion along such an orthogonal axis. The phases of these RF pulses are modulated with a quadratic time-dependence $\varphi_{RF}(t) = O_{i,180}t + \frac{R_{180}t^2}{2} + \varphi_0$ akin to that associated with the frequency sweep leading to Eq. 1, where φ_0 is an arbitrary initial phase, and the $G_{180}\hat{x}$ gradient is now blipped so as to apply integrated areas of $\Delta k_{180} = \frac{\gamma G_{180} T_{180}}{N_{180}}$ per blip, where N_{180} is the number of intervening sub-pulses. The main result of this combined RF/gradient manipulation will be the sculpting of a shape in the x-y plane. A consequence of the slow-domain RF discretization, however, will be the periodic replication of this profile along the low-bandwidth direction. This DANTE-like effect, which occurs for both the *k*- and SPEN-based discretized pulses [22, 27], can lead to sideband contributions arising from outside the region of interest (ROI). The spatial separation between these sidebands and the centerband in SPEN-based pulses will be $\Delta L = \frac{2\pi N_{180}}{\gamma T_{180} G_{180}}$ [22]. Therefore, avoiding band overlap requires the number of sub-pulses N_{180} to fulfill

$$\frac{N_{180}}{BW_{180} \cdot T_{180}} > 1 \Leftrightarrow N_{180} > BW_{180} \cdot T_{180} \qquad (2)$$

where $BW_{180} = \frac{O_{f,180} - O_{i,180}}{2\pi}$ is the chirped pulse bandwidth, with $O_{i,180}$ and $O_{f,180}$ the initial and final frequencies of the RF sweep. For simplicity one can assume that the sweep is centered on-resonance (i.e., $\Omega = 0$); the bandwidth of the sweep is then equal to $\frac{-O_{i,180}}{\pi}$. It follows from this that avoiding the appearance of excitation sidebands within the targeted ROI, will restrict the average gradient along the blipped dimension to

$$G_{180} < \frac{2\pi N_{180}}{\gamma ROI \cdot T_{180}} \qquad (3)$$

A clear separation between center- and side-band regions thereby limits the gradient that can be applied along the blipped dimension, a feature that when combined with their extended durations makes 2D pulses susceptible to field inhomogeneities and/or chemical shift misregistrations. This is a general feature of 2D RF pulses. One of the advantages of SPEN-based pulses over their k-space counterparts lies in the fact that, under suitable conditions, they allow one to exceed the gradient amplitude limit posed by Eq. 3 without causing leading to overlapping sidebands [22]. This is made possible by the sum of linear and quadratic phases that follow from the action of a chirped pulse. In order to eliminate the latter and enable a voxel-wide signal acquisition, 2D SPEN pulses add to their RF waveforms a continuous chirped pulse that eliminates the quadratic phases for both the centerband and the sidebands. Following

this refocusing pulse a linear term along the spatial dimension *x* will still remain in the phase of each band; thanks to differences in these linear phases among the different bands, their individual signals can be discriminated –and thereby selectively filtered out – even if their spatial regions overlap. For a readout acquisition this filtering could imply zeroing out all the readout samples, except for those *k*-values corresponding to the echo being sought. In a spectroscopic or imaging experiment one could then mask out the undesired sideband echoes, and recover solely the centerband's signal [22].

The present study exploits this feature, described for 2D pulses in Ref. [22], in order to achieve the excitation of complex shapes in three dimensions. Figures 1a and 1b show two ways in which this was implemented, both of them relying on pairs of discretized 2D SPEN-based pulses played consecutively along a shared "slow" dimension. If the encoding gradients, the RF duration and the number of sub-pulses are equal for both pulses, so will be their quadratic phases; this would give a chance to eliminate these unwanted phase terms, but at the same time it would make the remaining linear phase terms identical for all bands. Multiple excitation bands would then overlap, and it would not be possible to discriminate among them. To overcome this we explored three sideband-suppressing strategies that arise when concatenating two 2D SPEN-based pulses; namely,

- Utilizing equal effective encoding gradients and times, but different numbers of sub-pulses for the two discretized pulses. This will endow the pulses' centerbands with identical phase and amplitude profiles, but make the sidebands of the first 2D pulse fall in different spatial positions than the sidebands of the second. Indeed, recalling that the separation between excitation bands is $\Delta \mathrm{L} = \frac{2\pi \mathrm{N}_{180}}{\gamma \mathrm{T}_{180} \mathrm{G}_{180}}$, different number N_{180} of sub-pulses for two 2D SPEN pulses can lead to the elimination of linear and quadratic phase terms from the targeted ROI, but not from non-overlapping sidebands. Instances will arise, however, where sidebands corresponding to different harmonics of the first and second pulses may overlap; for these instances the quadratic phase terms will be cancelled, but unique linear terms will still remain. Thanks to these residual linear phase terms, the contribution from the side-excitations will still cancel out.
- Adjusting the RF duration and number of sub-pulses in both discrete SPEN-based pulses so that their replicates are similarly positioned, but their quadratic phase terms are not

canceled (e.g., by setting $N_{180}^{(2)} = 2N_{180}^{(1)}, T_{180}^{(2)} = 2T_{180}^{(1)}$). While this will not achieve the expected elimination of the ROI's quadratic phase, adding a continuous, short swept pulse designed to eliminate the residual quadratic term of the centerband while maintaining linear phase terms for the undesired sidebands, gives the possibility of removing the latter's contribution from the observed images. Indeed, being continuous, such third 180^0 pulse will have no harmonics and thus solely refocus the centerband. A version of such approach is introduced in Figure 1c.

- Another option that could do away with the additional chirp just mentioned consists of following an initial 2D discrete excitation pulse by a 2D discrete refocusing pulse lasting half the duration of the excitation, so as to mutually cancel the pulses' quadratic phases [28-30]. This scenario, as well as analogous ones encompassing chirped excitation and storage pulses, would add distinctive linear phases to the sidebands that would lead to their filtration. Unless making the initial excitation pulse exceedingly long, however, such strategies based on short 2D 180^0 pulses were found to exceed RF peak power limitations. Due to this reason we decided to focus only on the first two of the alternatives described.

Figure 2 presents insight arising from 1D Bloch simulations for the first two of these band-suppressing strategies, denoted as sequences I and II. Figure 2a shows results from a SPEN-based discrete-pulse simulation of sequence with $N_{180}^{(1)} = N_{180}^{(2)}$. As can be appreciated from the transverse phase profiles, the quadratic phases for all bands will be removed by the conclusion of the second 180^0 pulse (time point B^I). This leads to a constant phase value for both the centerband and the sidebands. In this state the centerband can be disentangled from the sidebands only if these do not overlap –a condition that is broken as G_{180} becomes stronger (Fig. 2a, right-most panel). Alternatively, the same sequence played out with a different number of sub-pulses (i.e., $N_{180}^{(1)} \neq N_{180}^{(2)}$, Fig. 2b) yields a clear reconstruction of the centerband with almost no traces of the sidebands. This is caused by the linear phase residuals affecting the sidebands at time point B^I, which leads to echoed signals from the centerband but not the sidebands (right-most column of Fig. 2b). A similar unfolding effect can be seen in Fig. 2c upon simulating sequence II, where a third chirped pulse added after the discretized pulses removes the undesired phase terms from the centerband but not from the sidebands (Fig. 2, time point C^{II}). These relaxation-free

simulations, performed assuming a uniform B_0 field, indicate that sequence II provides the best elimination of undesired sidebands, yet at the expense of adding a third refocusing pulse. In practice this will make sequence II longer –and therefore more susceptible to B_0 field inhomogeneities and relaxation-related signal losses– than its sequence I counterparts.

It is worth noting that all these sideband-suppressing strategies are not applicable to k-based 2D pulses, since then phases along all bands are constant rather than linear. Thus the limitation determined by Eq. 3 cannot be overcome for these pulses by any of these schemes.

3. Materials & Methods

Based on these considerations, the performance of SPEN-based and k-space-based pairs of 2D pulses for achieving 3D selectivity, was evaluated. All these experiments were carried out at 7 T using a Millipede® quadrature volume probe on a VNMRS® 300/89 vertical bore microimaging Varian system. Water phantom experiments were performed by implementing the sequences in Figures 1a and 1c, while *ex-* and *in vivo* tests were conducted using the slightly modified sequence in Figure 1b. RF and gradient waveforms for the 2D pulses were designed in Matlab® (The Mathworks, Natick, MA) using home-written routines. These waveforms were exported into the NMR scanner and clocked out with a 4 μs dwell time. Data processing was also performed off-line using home-written Matlab routines. All experiments started by drawing planar *x-y* and *x-z* contours that defined the desired 3D shape. Appropriate 2D pulses for imparting these contours were computed as described in [22], with the "slow" dimension of both the first and second 2D pulses chosen as the x axis. This was also chosen as the acquisition RO dimension, facilitating the removal of the sidebands' contributions. High-bandwidth, "fast" dimensions were set to y for the first 2D pulse and z for the second 2D pulse. For 2D SPEN-based pulses each sub-pulse along the "fast" dimension was calculated as a 1D Fourier transform (FT) of the corresponding row in the targeted spatial shape, and its amplitude was modulated by a WURST time-domain profile [31]. The frequency sweep along the "slow" (low-bandwidth) dimension was obtained by an overall phase modulation of the train of sub-pulses. For 2D *k*-based pulses, which covered a blipped Cartesian trajectory in k_x-k_y and k_x-k_z excitation spaces, the sub-pulses' RF was computed using 2D Fourier analyses of the desired spatial patterns. These targeted 2D patterns were smoothed with a 2D Gaussian kernel, prior to either their SPEN- or *k*-based RF waveform designs. Both SPEN- and *k*-based pulses also used a flyback scheme [32], whereby RF was only played out during the plateau of the odd

k-lines in an asymmetric zig-zag gradient waveform. Such procedure was needed to compensate for eddy-current timing errors, difficult to correct on the utilized vertical magnet. All 2D refocusing pulses were flanked by crusher gradients. Re-phasing and pre-phasing gradients were also applied on both sides of the second refocusing 2D pulse (simultaneously with the crusher gradients) to account for dephasing caused by the "fast" gradients of the 2D pulses. The 2D pulses used for animal-oriented scans were shorter than the ones used for the *in vitro* experiments to account for the shorter relaxation times of biological tissues; (13 and 19 ms were the practical ranges for 2D pulses in *in*- and *ex vivo* experiments, respectively. In the case of 2D SPEN-based refocusing pulses, the probe's maximal RF handling power (150W, corresponding to a ca. 32 μs hard 90˚ pulse) was used for refocusing. For *k*-based 2D pulses, this power wasn't high enough to obtain a flip angle of 180^0 at pulse durations that were realistically short for *ex*- and *in-vivo* operation; in these experiments, pulse angles of 120^0 were used.

To test the achieved localization, experiments incorporated a 3D *k*-space multi-scan image acquisition scheme. For the water phantom experiments, each scan had a unique k_y/k_z phase encoding following a full-volume excitation, while k_x was sampled using a conventional G_{RO} readout. A slice-selective excitation pulse and a single phase encoding was also explored in the *ex*- and *in-vivo* tests (Fig. 1b). Water tube phantom images were 2D phase-encoded and reconstructed using a 3D inverse Fourier transform (FT); the multi-slice 2D *ex*- and *in-vivo* acquisitions were reconstructed using a 2D inverse FT. When needed to be masked, sideband contributions to the reconstructed images were eliminated by zeroing all the *x* readout measurements except for the 50 central samples. The echo times used were 59-70 ms for the phantom tests, 36-42 ms for the *ex-vivo* sample and 33ms for the *in-vivo* experiment.

The most basic of the analyzed phantoms was a 15 mm inner diameter tube filled with $CuSO_4$-doped water. The *ex vivo* sample was a rat brain immersed in Fluorinert®, which provides susceptibility matching and reduces field inhomogeneities. *In vivo* experiments targeted the brain of a mouse. For these experiments, an anesthesia system mixing 1–2% Isoflurane and oxygen gas was fed for respiration through a dedicated nose mask, at ca. 1 L/min. During anesthesia, the respiration signal from a sensor attached to the animal's chest was monitored. A dedicated heating system was also built and used to keep the animal's body temperature stable. Animal protocols and maintenance were in accord with the guidelines of the Committee on Animals of the Weizmann Institute of Science and were approved by this Committee. Prior to all experiments, localized shimming was done with PRESS [7].

4. Results

In general, applying the sequences in Fig. 1 gave images exhibiting several replicas along the readout dimension, here chosen as the "slow" dimension of the 2D pulses. In cases where the excited sidebands did not overlap with the centerband these echoes could be easily discerned and separated, enabling the centerband's ROI reconstruction. Examples of this are illustrated in Figures 3a and 3b for carvings of 3D shapes from within a water tube, using *k*- and SPEN-based pairs of 2D pulses, respectively. In all these scenarios the desired 3D shape was identical: a diamond shape in x-y intersecting with a diamond along x-z. Following these excitations, the selected regions were imaged by 3D MRI acquisitions with full 2D phase encoding. Notice that while of a "grainer", coarser nature than its *k*-based counterpart, already at this stage the SPEN-based images exhibit fewer distortions from field inhomogeneities and/or eddy currents. Further distortions in the images elicited by the *k*-based pulses probably arise from RF design errors associated to the use of the small-tip-angle approximation in these large-flip-angle k-based experiments –design errors that will be less important in adiabatic sweeps like those underlying the SPEN-based pulses. As stronger gradients were used and side- and center-band echoes interfered with one another, the ROI could not be reconstructed from these simple experiments. As mentioned,, this complication could be resolved in the SPEN-based sequences by either: (i) applying 2D pulses with a different number of sub-pulses $N_{180}^{(1)} \neq N_{180}^{(2)}$, or (ii) concatenating a continuously swept pulse to the pair of 2D pulses, even if these had an equal number of sub-pulses $N^{(1)} = N^{(2)}$. Either of these strategies led to a separation along the acquisition readout, of otherwise overlapping side- and center-band echoes. For instance, Figure 3c implements the sequence in Fig. 1a on a water tube, while incorporating an unfolding technique based on setting $N_{180}^{(1)} \neq N_{180}^{(2)}$. This enabled doubling the encoding gradient along the SPEN dimension compared to that in Fig. 3b, affording sharper spatial resolutions along the low bandwidth dimension while remaining free from blipped-related sidebands. We ascribe the better results observed with the SPEN-based pulses in Fig. 3c over their counterparts in Figs. 3a and 3b to an increased immunity to B_0 inhomogeneities, associated to a doubling of the G_{180}.

Figure 4 presents additional aspects of these folding and unfolding features, focusing on the properties observed along the SPEN dimension when the constraints set by Eq. 3 on the 2D SPEN gradient G_{180} for avoiding band overlap, are broken. Shown in Fig. 4a are the results arising upon increasing the amplitude of this slow gradient to $\mathrm{G}_{180} = \frac{3 \cdot 2\pi N_{180}}{\gamma \mathrm{ROI} \cdot \mathrm{T}_{180}}$; when using $N_{180}^{(1)} = N_{180}^{(2)}$ the overlap

between the ROI and two undesired sidebands, is evident. Figure 4b shows how the ROI can be cleaned up while keeping the same G_{180} by using $N_{180}^{(1)} \neq N_{180}^{(2)}$. Figure 4c, collected with a $G_{180} = \frac{2 \cdot 2\pi N_{180}^{(1)}}{\gamma ROI \cdot T_{180}}$ that is four times larger than the bound in Eq. (3), illustrates the selection that can be achieved even when $N_{180}^{(1)} = N_{180}^{(2)}$, by appending a continuous 180˚ adiabatic sweep to the 2D pulses. This band selectivity, however, is achieved at the expense of an additional evolution time that leads to a decay-driven "rounding off" of the targeted shape.

Figure 5 displays an analogous set of results, collected on an *ex vivo* rat brain. These images show, in addition to 3D selectivity, anatomical details that assist in validating the localization and delineation of the targeted tissue. In Fig. 5a the *x-y* shape was drawn according to the edges exhibited by the corpus callosum in the equator slice (where z=0); Fig. 5b targeted only the left hemisphere of the corpus callosum, while Fig. 5c targeted the right hemispheric part of the corpus callosum. Notice in all images the good preservation of hypointense features in the selected regions. Such *ex vivo* measurements could not be repeated with 2D k-based pulses: RF peak power limitations led to pulse durations that were too long (30ms) for this biological tissue, and to flip angles that were much lower than the full, ideal inversion. These long pulses and compromises in the full inversions, led to very poor sensitivity and to unsuitable images even after prolonged scan times.

Figure 6 presents results arising from the sequence in Fig. 1b, when applied *in vivo* to a mouse brain. The manually selected 3D shape was a horse-shoe ROI around the corpus callosum in *x-y*, and an oval in *x-z*. The selectivity achieved along all three axes is clearly visible. Anatomical details, however, are more blurred than in the *ex vivo* results of Figure 5. We tentatively ascribe this to signal decays related to motions that were absent in the *ex vivo* cases. In addition, there are some weak contributions from sidebands at z=0 and z=0.5cm, positioned in the lower part of the images along the discretized SPEN dimension. Still, the centerband echo was easily distinguishable to filter out most of the sidebands, and delivers a clear view of the selected brain region's ROI. Such results could not be recapitulated when assaying sequences relying on 2D *k*-based pulses.

5. Discussion

This study evaluated a number of methods for selecting complex 3D shapes based on pairs of 2D excitation and/or refocusing pulses. While less general than a full 3D RF pulse, these planar

manipulations have the advantage of being short while providing a fair amount of spatial selectivity. Another useful feature is their triggering by a non-coding pulse, which can be easily adapted to spectrally-selective excitations and thus provide an initial degree of chemical shift selectivity. This strategy can be exploited in instances where imaging capabilities are limited as in hyperpolarized ^{13}C MRS [33, 34], or when targeting very small objects like lymph nodes by ^{1}H MRS [35]. The performance of pairs of 2D SPEN-based *x-y/x-z* pulses was compared to the 3D selectivity achieved with a pair of 2D k-based pulses. For a water phantom the latter sequence gave more distorted and blurred images, even under relatively homogenous B_0 fields. A similar behavior is evidenced by simulations (see Supplementary Material), which evidence that they are largely due to broken assumptions in the small-tip-angle approximation. A feature aiding the SPEN-based implementation of this sculpting, rest on the fact that the gradient along these pulses' "slow" dimension could be significantly increased relative to the limits needed for separating sidebands from centerbands (Eq. 3). To enable the use of these stronger gradients "unfolding" techniques had to be developed; for instance, concatenating different numbers of sub-pulses for the first and second 2D RF shapes. This provided a clean separation between the center- and the side-band contributions; in general, setting the "slow" gradient strength to $G_{180} = 2\frac{2\pi N_{180}^{(1)}}{\gamma ROI \cdot T_{180}}$, provided the best tradeoff between a higher robustness to field inhomogeneities, versus an ability to fully null the sideband contributions in the final reconstruction.

The advantage of imprinting 3D selectivity with SPEN-based 2D pulses, was especially evident under *ex-* and *in-vivo* conditions. For the *k*-based tests no reasonably complex shape could be sculpted in these scenarios, reflecting an increased sensitivity towards field inhomogeneities, coupled to non-idealities arising when designing *k*-based 2D 180^0 pulses on the basis of the small-tip-angle approximation. In this respect it was surprising to see how useful this approximation –valid for a small-angle excitation and a magnetization vector starting at M_z – was for the design of the 2D SPEN-based 180^0 pulses. The right selectivity delivered by this Fourier based design was verified by 2D Bloch simulations (see Supplementary Material). The performance of this simple approach remains to be compared against more sophisticated 'inherently refocused' pulses that can achieve large tipping angles [35], and against pulses designed using non-linear Shinnar-Le Roux algorithms that can deliver accurate profiles even for large tip angles [36-40].

While it was satisfying to witness the usefulness of the SPEN-based 3D shaping pulses in tissues, the *in vivo* selectivity and boundary definition was not as sharp as for the *ex vivo* experiments. We ascribe

this to the stronger motional losses arising in the former case during the relatively long pulses. Indeed, prolonged durations are still a feature associated to the use of these pairs of 2D RF pulses. A better definition should arise if applying the RF on both even and odd encoding gradient echoes; i.e., if working during both positive and negative plateaus of the "fast" gradient waveform. This could shorten the pulses or halve the delays between the sub-pulses, thus shifting the sidebands away from the centerband and enabling a further increase in the amplitude of G_{180}. This was technically not possible in our system due to eddy currents, but may be suitable in better-behaved gradient systems. Other options to shorten the 2D pulses include parallel transmission [41, 42] and interleaving multiple scans along the fast sculpting dimension [43]. Such approaches, which so far have been essential to enable *k*-based schemes to select 3D shapes, could also shorten the total duration of the SPEN-based 2D pulses, albeit at the price of doubling the number of scans and of increasing the required RF power. Finally, in cases where T_2 or T_2^* degrade too much the sharpness of the *in vivo* selectivity and image contrast delivered by the sculpting pulses described here, one may also consider the use of sequences involving 2D SPEN pulses that suppress 3D volume shapes outside the targeted shape. When followed by a broadband excitation, the latter could then be used for targeting a preselected ROI.

6. Conclusions

Exciting complex 3D shapes could be a useful complement in functional, relaxation, diffusion or spectroscopic measurements, particularly in cases were sensitivity is compromised, or partial volume effects are detrimental. This study compared two techniques for achieving complex 3D volume localizations: one based on 2D SPEN-based pulses and the other on *k*-based 2D pulses. While not completely general, this approach was the most robust among the strategies tested and covers a variety of shapes required to perform flexible tissue localization. In *in vitro* experiments localization could be achieved by both of the assayed routes, yet in *ex*- and *in-vivo* tests, 3D volume selectivity was only delivered by SPEN-based pulses. Factors assisting in this improved performance SPEN's accommodation of stronger encoding gradients along the "slow" dimension, and "unfolding" techniques designed to deliver a clear echo from the targeted ROI while suppressing excitation sidebands. This delivered a tool capable to excite complex-shaped 3D regions *in vivo*, in a single scan and without parallel transmission. Future research should explore the potential of the ensuing method in physiological investigations, and the incorporation of alternative spatiotemporally encoding strategies.

Acknowledgments. We are grateful to Amir Seginer for useful discussions and to Koby Zibzener for supporting the experimental setup. This work was supported by the Kimmel Institute for Magnetic Resonance (Weizmann Institute), the Israel Science Foundation grant 795/13, and the generosity of the Perlman Family Foundation.

REFERENCES

[1] W. Weber-Fahr, M. G. Busch and J. Finsterbusch, "Short-echo-time magnetic resonance spectroscopy of single voxel with arbitrary shape in the living human brain using segmented two-dimensional selective radiofrequency excitations based on a blipped-planar trajectory," *Magn. Reson. Imaging,* vol. 27, no. 5, p. 664–671, 2009.

[2] J. Snyder, M. Haas, I. Dragonu, J. Hennig and M. Zaitsev, "Three-dimensional arbitrary voxel shapes in spectroscopy with submillisecond TEs," *NMR in Biomed.,* vol. 25, no. 8, p. 1000-1006, 2012.

[3] Q. Qin, J. C. Gore, . R. A. de Graaf and . M. D. Does, "Quantitative T2 measurement of a single voxel with arbitrary shape using pinwheel excitation and CPMG acquisition," *MAGMA,* vol. 20, no. 5-6, p. 233-240, 2007.

[4] S. C. Partridge, L. Singer, R. Sun, L. J. Wilmes, C. S. Klifa, C. D. Lehman and N. M. Hylton, "Diffusion-weighted MRI: influence of intravoxel fat signal and breast density on breast tumor conspicuity and apparent diffusion coefficient measurements," *Magn. Reson. Imaging,* vol. 29, no. 9, p. 1215–1221, 2011.

[5] P. Christiansen, O. Henriksen, M. Stubgaard, P. Gideon and H. B. Larsson, "In Vivo Quantification of Brain Metabolites by 1H-MRS Using Water as an Internal Standard," *Magn. Reson. Imaging,* vol. 11, no. 1, p. 107-118, 1993.

[6] R. Mekle, V. Mlynarik, G. Gambarota, M. Hergt, G. Krueger and R. Gruetter, "MR Spectroscopy of the Human Brain With Enhanced Signal Intensity at Ultrashort Echo Times on a Clinical Platform at 3T and 7T," *Magn. Reson. Med.,* vol. 61, p. 1279-1285, 2009.

[7] P. A. Bottomley, "Spatial Localization in NMR Spectroscopy in Vivo," *Ann. N.Y. Acad. Sci.,* vol. 508, p. 333–348, 1987.

[8] V. Mlynarik, G. Gambarota, H. Frenkel and R. Gruetter, "Localized Short-Echo-Time Proton MR Spectroscopy With Full Signal-Intensity Acquisition," *Magn. Reson. Med.,* vol. 56, p. 965–970, 2006.

[9] Q. Qin, J. C. Gore, M. D. Does, M. J. Avison and R. A. de Graaf, "2D Arbitrary Shape-Selective Excitation Summed Spectroscopy (ASSESS)," *Magn. Reson. Med.,* vol. 58, no. 1, p. 19-26, 2007.

[10] P. A. Bottomley and C. J. Hardy, "Two-dimensional spatially selective spin inversion and spin-echo refocusing with a single nuclear-magnetic-resonance pulse," *J. Appl. Phys.,* vol. 62, p. 4284–4290, 1987.

[11] S. Rieseberg, J. Frahm and J. Finsterbusch, "Two-Dimensional Spatially Selective RF Excitation Pulses in Echo-Planar Imaging," *Magn. Reson. Med.,* vol. 47, p. 1186–1193, 2002.

[12] S. Saekho, F. E. Boada, D. C. Noll and A. V. Stenger, "Small Tip Angle Three-Dimensional Tailored Radiofrequency Slab-Select Pulse for Reduced B1 Inhomogeneity at 3 T," *Magn. Reson. Med.,* vol. 53, p. 479–484, 2005.

[13] C.-y. Yip, J. A. Fessler and D. C. Noll, "Advanced Three-Dimensional Tailored RF Pulse for Signal Recovery in T2*-Weighted Functional Magnetic Resonance Imaging," *Magn. Reson. Med.,* vol. 56, p. 1050–1059, 2006.

[14] J. T. Schneider, R. Kalayciyan, M. Haas, S. R. Herrmann, W. Ruhm, J. Hennig and P. Ullmann, "Inner-Volume Imaging In Vivo Using Three-Dimensional Parallel Spatially Selective Excitation," *Magn. Reson. Med.,* vol. 69, p. 1367–1378, 2013.

[15] A. C. Zelinski, L. M. Angelone, V. K. Goyal, G. Bonmassar, E. Adalsteinsson and L. L. Wald, "Specific Absorption Rate Studies of the Parallel Transmission of Inner-Volume Excitations at 7T," *Magn. Reson. Imaging,* vol. 28, p. 1005-1018, 2008.

[16] N. Ben-Eliezer, Y. Shrot and L. Frydman, "High-definition single-scan 2D MRI in inhomogeneous fields using spatial encoding methods," *Magn. Reson. Imaging,* vol. 28, p. 77–86, 2010.

[17] A. Tal and L. Frydman, "Single-scan multidimensional magnetic resonance," *Prog. Nucl. Magn. Reson. Spectrosc.,* vol. 57, no. 3, p. 241-292, 2010.

[18] L. Frydman, A. Lupulescu and T. Scherf, "Principles and Features of Single-Scan Two-Dimensional NMR Spectroscopy," *J. Am. Chem. Soc.,* vol. 125, p. 9204-9217, 2003.

[19] Y. Shrot and L. Frydman, "Spatially-Encoded NMR and the Acquisition of 2D Magnetic Resonance Images Within a Single Scan," *J. Magn. Reson.,* vol. 172, p. 179-190, 2005.

[20] L. Frydman, T. Scherf and A. Lupulescu, "The Acquisition of Multidimensional NMR Spectra Within a Single Scan," *Proc. Natl. Acad. Sci. USA,* vol. 99, p. 15858-15862, 2002.

[21] R. Chamberlain, J.-Y. Park, C. Corum, E. Yacoub, K. Ugurbil, C. R. Jack and M. Garwood, "RASER: A new ultrafast magnetic resonance imaging method," *Magn. Reson. Med.,* vol. 58, p. 794-799, 2007.

[22] J. N. Dumez and L. Frydman, "Multidimensional Excitation Pulses Based on Spatiotemporal Encoding Concepts," *J. Magn. Reson.,* vol. 226, p. 22-34, 2013.

[23] A. L. S. Snyder, C. A. Corum, S. Moeller, N. J. Powell and M. Garwood, "MRI by Steering Resonance Through Space," *Magn. Reson. Med.,* vol. 72, p. 49–58, 2014.

[24] A. Tal and L. Frydman, "Spatial encoding and the single-scan acquisition of high definition MR images in inhomogeneous fields," *J. Magn. Reson.,* vol. 182, p. 179-194, 2006.

[25] G. Morris and R. Freeman, "Selective excitation in Fourier-transform nuclear magnetic-resonance," *J. Magn. Reson.,* vol. 29, p. 433-462, 1978.

[26] R. Freeman, Spin choreography: basic steps in high resolution NMR, University Sciences Books: Sausalito, CA, 1997.

[27] S. Conolly, J. Pauly, D. Nishimura and A. Macovski, "Two-Dimensional Selective Adiabatic Pulses," *Magn. Reson. Med.,* vol. 24, p. 302-313, 1992.

[28] J. Bohlen, M. Rey and G. Bodenhausen, "Refocusing with chirped pulses for broadband excitation without phase dispersion.," *J. Magn. Reson.,* vol. 84, p. 191-197, 1989.

[29] A. Tal, B. Shapira and L. Frydman, "A continuous phase-modulated approach to spatial encoding in ultrafast 2D NMR spectroscopy," *J. Magn. Reson.,* vol. 176, p. 107-114, 2005.

[30] N. S. Andersen and W. Köckenberger, "A simple approach for phase-modulated single-scan 2D NMR spectroscopy," *Magn. Reson. Chem.,* vol. 10, p. 795–797, 2005.

[31] E. Kupce and R. Freeman, "Adiabatic pulses for wide-band inversion and broadband decoupling," *J. Magn. Reson. A,* vol. 115, p. 273–276, 1995.

[32] A. Z. Lau, A. P. Chen, R. E. Hurd and C. H. Cunningham, "Spectral–spatial excitation for rapid imaging of DNP compounds. NMR in biomedicine," *NMR Biomed.,* vol. 24, no. 8, p. 988-996, 2011.

[33] K. Golman, R. i. Zandt and M. Thaning, "Real-time Metabolic Imaging," *Proc. Natl. Acad. Sci.USA ,* vol. 103, no. 30, p. 11270–11275, 2006.

[34] S. E. Day, M. I. Kettunen, M. K. Cherukuri, J. B. Mitchell, M. J. Lizak, H. D. Morris, S. Matsumoto, A. P. Koretsky and K. M. Brindle, "Detecting Response of Rat C6 Glioma Tumors to Radiotherapy Using Hyperpolarized [1-13C]Pyruvate and 13C Magnetic Resonance Spectroscopic Imaging," *Magn. Reson. Med.,* vol. 65, p. 557-563, 2011.

[35] J. Pauly, D. Nishimura and A. Macovski, "A Linear Class of Large-Tip-Angle Selective Excitation Pulses," *J. Magn. Reson.,* vol. 82, p. 571-587, 1989.

[36] J. Pauly, P. Le Roux, D. Nishimura and A. Macovski, "Parameter Relations for the Shinnar-Le Roux Selective Excitation Pulse Design Algorithm," *IEEE Trans. Med. Imaging,* vol. 10, no. 1, 1991.

[37] C. Ma and Z.-P. Liang, "Design of Multidimensional Shinnar–Le Roux Radiofrequency Pulses," *Magn. Reson. Med.,* vol. 73, p. 633–645, 2015.

[38] R. F. Schulte, J. Tsao, P. Boesiger and K. P. Pruessmann, "Equi-ripple design of quadratic-phase RF pulses," *J. Magn. Reson.,* vol. 166, p. 111-122, 2004.

[39] P. Balchandani, J. Pauly and D. Spielman, "Designing adiabatic radio frequency pulses using the Shinnar–Le Roux algorithm," *Magn. Reson. Med.,* vol. 64, no. 3, p. 843-851, 2010.

[40] J. Pauly, D. Spielman and A. Macovski , "Echo-Planar Spin-Echo and Inversion Pulses," *Magn. Reson. Med.,* vol. 29, p. 776–782, 1993.

[41] U. Katscher, P. Bornert, C. Leussler and J. S. van den Brink, "Transmit SENSE," *Magn. Reson. Med.,* vol. 49, p. 144-150, 2003.

[42] Y. Zhu, "Parallel Excitation With an Array of Transmit Coils," *Magn. Reson. Med.,* vol. 51, p. 775–784, 2004.

[43] M. Takizawa, H. Hanada, K. Oka, T. Takahashi, E. Yamamoto and M. Fujii, "A Robust Ultrashort TE (UTE) Imaging Method With Corrected k-Space Trajectory by Using Parametric Multiple Function Model of Gradient Waveform," *IEEE Trans. Med. Imaging,* vol. 32, no. 2, 2013.

[44] P. T. Callaghan, Principles of Nuclear Magnetic Resonance Microscopy, Oxford University Press, 1991.

[45] J. M. Star-Lack, E. Adalsteinsson, M. F. Adam, D. J. Terris, H. A. Pinto, J. M. Brown and S. M. Daniel , "In Vivo 1H MR Spectroscopy of Human Head and Neck Lymph Node Metastasis and Comparison with Oxygen Tension Measurements," *Am. J. Neuro.,* vol. 21, p. 183-193, 2000.

7. Figure captions

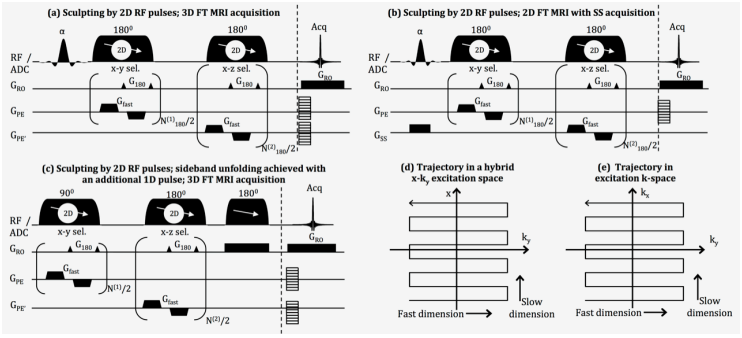

Figure 1. (a, b) Pulse sequences considered for imparting 3D spatial selectivity using pairs of 2D RF pulses. Following a broadband or selective excitation pulse α a 2D refocusing pulse selects a shape in *x-y* whereas a subsequent 2D pulse selects a shape in *x-z*. The acquisition that follows is intended for 3D k-space imaging, where each shot acquires a line along k_x with a different k_y/k_z phase encoding (a), or performs a slice-selective excitation (b). The imaging block can be replaced by a FID acquisition for NMR spectroscopy. (c) 3D sculpting strategy suitable for SPEN-based strategies where the excitation/refocusing 2D pulse pair is followed by a continuous 1D swept pulse in order to remove excitation sidebands (see text). (d) Hybrid SPEN-Fourier trajectory in the x/k_y–space imparted by the SPEN-based pulses in (a-c). (e) Idem but for 2D k-based pulses. The association of the imaging directions RO,PE,PE' with x,y,z, is arbitrary and for illustrative purposes only.

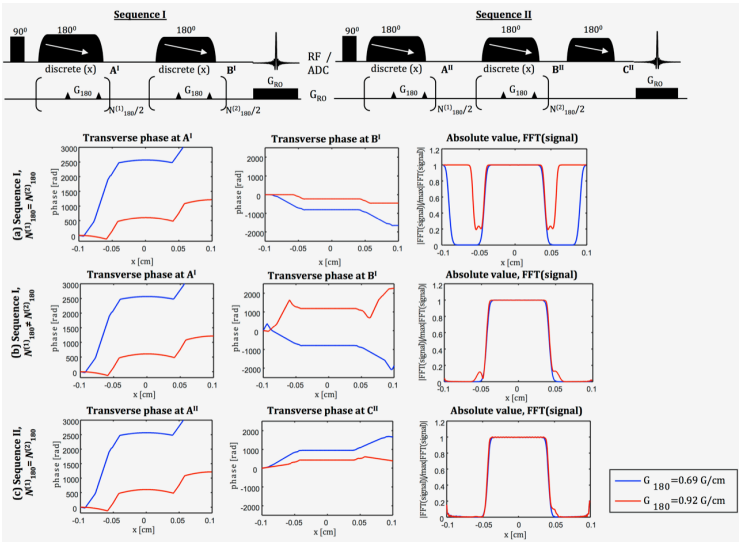

Figure 2. Bloch simulations showing the effects of the SPEN-based sequences I and II, calculated assuming a single (x) spatial dimension. The plots present transverse magnetization phase profiles after the first discrete pulse (left column) and after a full refocusing (middle column) occurring at point B^{I} for sequence I and at point C^{II} for sequence II. The right hand column displays the final spatial magnetization profiles excited, for gradient strengths leading to a strong (red) / weak (blue) band overlap. (a) Results of sequence I acting devoid of unfolding strategies, and arising from an identical number of sub-pulses for both 180^0 sweeps $\left(N_{180}^{(1)} = N_{180}^{(2)} = 128\right)$. The encoding gradients of the discrete pulses were also identical and defined as: $G_{180}^{(1)} = G_{180}^{(2)} = \frac{BW_{180}}{FOV} = \frac{N_{180}}{FOV \cdot T_{180}}$ (0.92 G/cm) for the red curve and $G_{180}^{(1)} = G_{180}^{(2)} = \frac{0.75BW}{FOV}$ (0.69 G/cm) for the blue curve, respectively. (b) Same as (a) but with the unfolding achieved by using a different number of sub-pulses, $\frac{N_{180}^{(2)}}{N_{180}^{(1)}} = \frac{170}{128}$, for each discrete pulse. The encoding gradients of the discrete pulses were set-up so as to have the same total k areas. (c) Results of sequence II, where spins are not fully refocused after the second discrete pulse, but the remaining quadratic phase is removed by a continuous refocusing chirp added after the second discrete chirp. The second and third chirped pulses' durations were $T_{180}^{(2)}$=1.33 $\cdot$ $T_{180}^{(1)}$ and 0.82 $\cdot$ $T_{180}^{(1)}$ respectively; the discrete pulses had $N_{180}^{(1)}$=128 , $N_{180}^{(2)}$=170 sub-pulses.

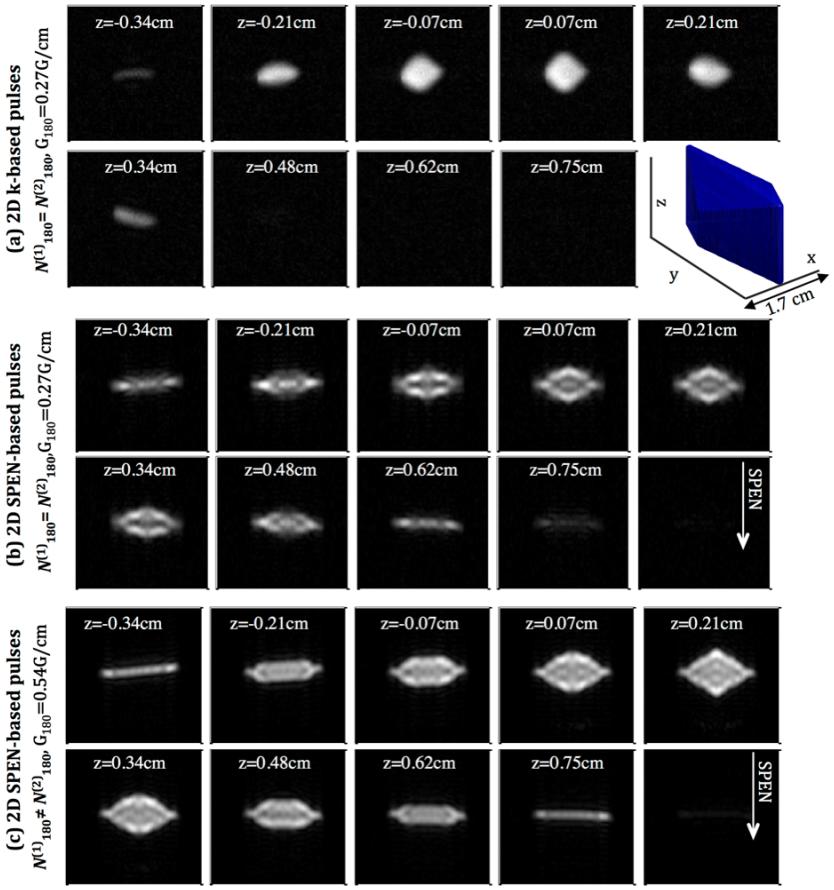

Figure 3. 3D spatial selectivity demonstrated on a water test tube using the sequence in Figure 1a, recorded under identical, high-resolution shimming conditions (15 Hz full-width-half-height widths measured in PRESS experiments including the relevant voxel). The selected ROI was an intersection of diamonds in *x-y* and in *x-z* (illustration in the lower right panel of a). **(a)** 2D k-based pulse results. **(b) and (c)** 2D SPEN-based pulses results. G_{180} was 0.27 G/cm in (a,b) and 0.54 G/cm in (c). G_{180} led to overlapping center- and sidebands in (c), which were suppressed by setting $N^{(1)}_{180} \neq N^{(2)}_{180}$. Parameters were equal in all other aspects. For (a) and (b) the 2D concatenated pulses used $N^{(1)}_{180} = N^{(2)}_{180} = 64$; in (c) $N^{(1)}_{180} = 64, N^{(2)}_{180} = 85$. In all cases 2D pulses were 32.8 ms long. The 2D SPEN-based pulses swept over a bandwidth of 1.95kHz in (b) or 3.9kHz in (c), corresponding to a region of 1.7cm along the SPEN dimension, at a sweep rate of R = 59.5 kHz/s (b) or 119 kHz/s (c). Their $\gamma B_{1,max}/2\pi$ was 9kHz, yielding an adiabaticity factor $Q = \frac{\gamma B_1^{max}}{\sqrt{R}} =$ 36.9 (b) or 26 (c). 64x16x256 samples were imaged along k_y, k_z, and k_x respectively, covering a Field-of-View of 2.2cm x 2.2cm x 2.2cm. Ten axial images are displayed –9 for (a) as no data show beyond the 7th panel– out of sixteen that were acquired.

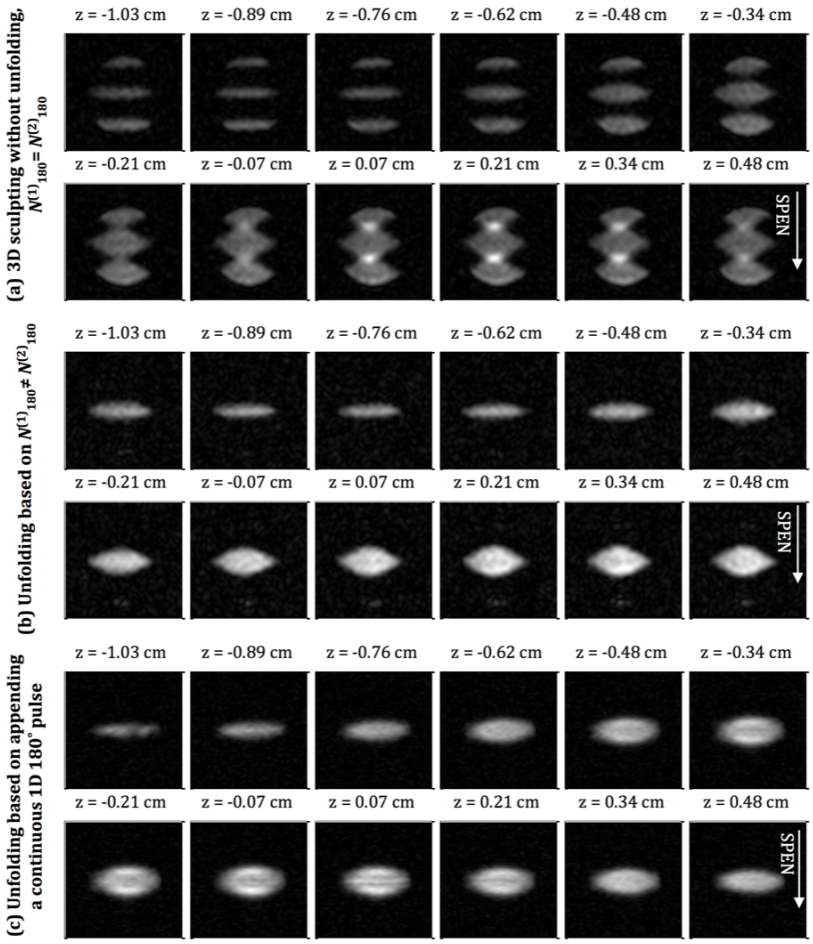

Figure 4. 3D spatial selectivity demonstrated on a water tube with SPEN-based 2D pulses according to the schemes in Fig. 1, with and without unfolding, targeting the same diamond shape as in Figure 3. **(a)** Sculpting with a pair of refocusing SPEN-based 2D pulses without unfolding: $N_{180}^{(1)} = N_{180}^{(2)} = 54$. **(b)** Similar to (a) but upon canceling sidebands with the scheme in Figure 1a, with $N_{180}^{(1)} = 54, N_{180}^{(2)} = 72$. **(c)** Sideband suppression implemented according to Fig. 1c, where a 180^0 continuously swept pulse is added subsequent to a pair of 2D pulses with $N^{(1)} = N^{(2)} = 36$. In (a) and (b) the encoding gradient G_{180} was 0.8 G/cm, *i.e.* three times higher than the constraint set by Eq. 3. In (c) it was 0.54 G/cm, i.e. twice this limit; these gradient amplitudes correspond to swept bandwidths of 5.8 kHz (a-b) / 3.9 kHz (c). The 2D pulses durations were $T_{180}^{(1)}$=$T_{180}^{(2)}$ =27.6 ms for (a-b) and $T_{90}^{(1)} = T_{180}^{(2)} = T_{180}^{(3)}$ =18.4 ms for (c) , where $T_{180}^{(3)}$ was the duration of the continuously swept pulse. The total RF irradiation time of the swept pulses in (a,b) and (c) was matched, in the sense that the 2D pulses durations $T_{180}^{(1)} + T_{180}^{(2)}$in (b) was set equal to $T_{90}^{(1)} + T_{180}^{(2)} + T_{180}^{(3)}$ in (c). Sweep rates for (a-c) were 212 kHz/s, the 2D pulses had a $\gamma B_{1,max}/2\pi = 9$ kHz and an adiabaticity factor Q = 19.5. The 2D pulses covered a region of 1.7x1.7 cm along the SPEN and Fourier dimensions. A full 3D k-space acquisition similar as in Fig. 3 was done, except for the maximum k_z that was here doubled.

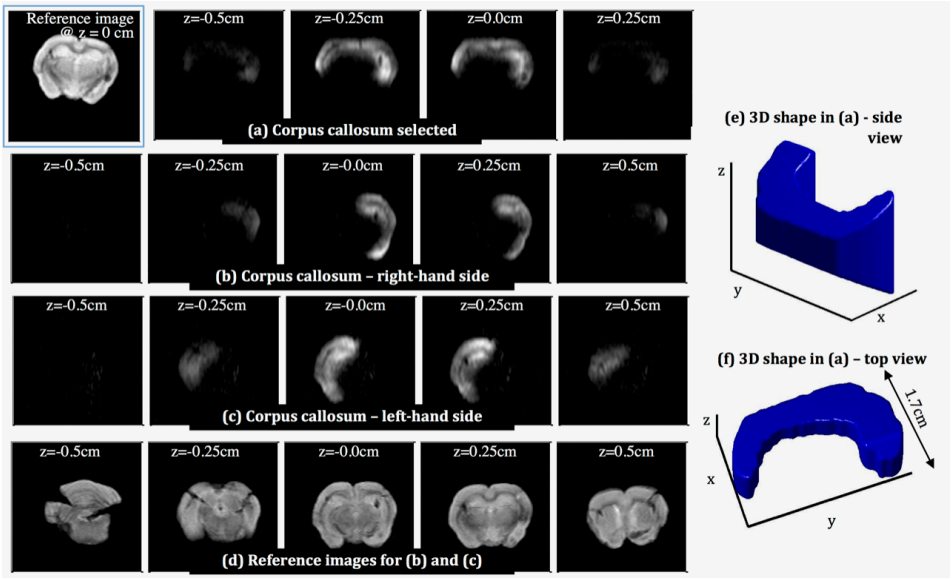

Figure 5. SPEN-based 3D spatial selectivity demonstrated in an *ex vivo* rat brain. Spin-echo axial images were acquired with the sequence in Fig. 1b using a slice thickness of 2 mm, 64x256 points per slice, an acquisition time $T_a = 1024$ μs, an acquisition bandwidth of 250 kHz, and a TR of 2 s. **(a)** Selected volume given by the intersection of a manually drawn callosal ROI in *x*-*y* and a tapered diamond in *x*-*z*. The left-most image shows a non-selective reference for $z = 0$. **(b,c)** Selected shapes involving manually selecting the left and the right *x*-*y* ROIs in (a), respectively. **(d)** Non-selective reference images for experiments in (b) and (c), acquired by turning off the pulse-related gradients. **(e,f)** Surface rendering (side and top views) of the 3D shape selected in (a). In (a,c) every 2D pulse was 13.8 ms long with $N_{180}^{(1)} = 26, N_{180}^{(2)} = 36$. G_{180} was 0.54G/cm, twice the limit to avoid centerband folding. In (b) the 2D pulses were 18.4ms long with $N_{180}^{(1)} = N_{180}^{(2)} = 36$ and centerband unfolding was unnecessary. The 2D pulses swept over a frequency range of 3.9 kHz in (a,c) and 2.9 kHz in (b), covering a region of 1.7 cm along the "slow" dimension at a sweep rate of 283 kHz/s in (a,c) and 158 kHz/s in (b). The 2D pulses had a $\gamma B_{1,max}/2\pi$ of 9kHz and adiabaticity factors Q=16.9 in (a,c) and 22.6 in (b). Eight averages were collected for (a), 4 averages for (b) and (c). The sample position was slightly different in (a) than in (b-d).

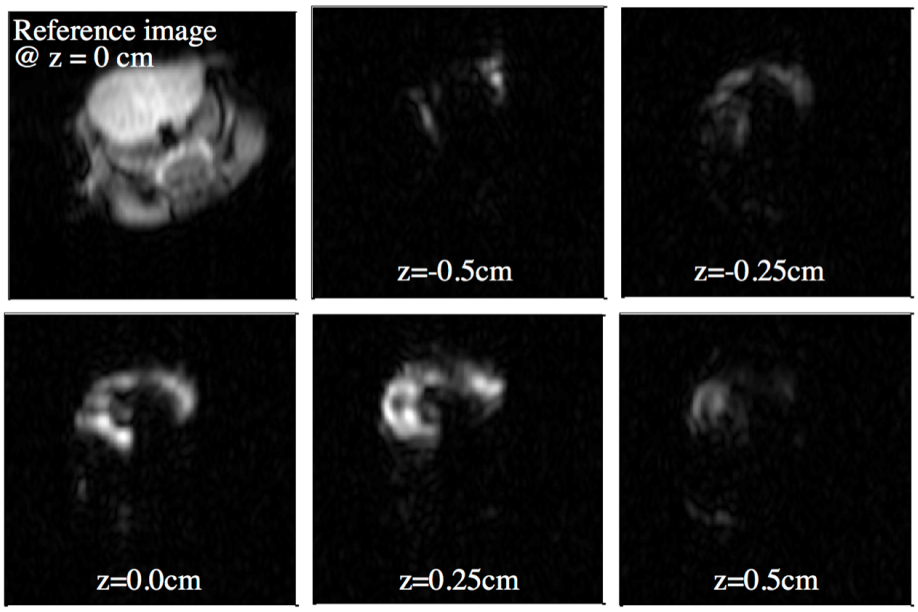

Figure 6. 3D spatial selectivity evidenced by the sequence in Fig. 1b, on an *in vivo* mouse brain. Five spin-echo axial images from z=-0.5 cm to z=0.5 are presented. The left-most image on the top shows a non-selective reference image for the z=0 slice. The desired volume was defined by a manually drawn ROI around the corpus callosum in x-y, and an oval in x-z. The two 2D SPEN-based pulses were 13.8ms long with $N_{180}^{(1)} = 26, N_{180}^{(2)} = 36$; this implemented an unfolding of the centerband ROI even for $G_{180} = \frac{2 \cdot 2\pi N_{180}^{(1)}}{\gamma ROI_{180} T_{180}} = 0.54\ G/cm$. The 2D pulses swept a frequency range of 3.9 kHz, covering a FOV of 1.7 cm at a sweep rate of 283 kHz/s with a $\gamma B_{1,max}/2\pi = 9$kHz, yielding an adiabaticity factor Q = 16.9. The reference non-selective image was acquired by turning off the pulse-related gradients. Four averages per *k*-point were acquired with a {0°,180°} phase cycling of the excitation pulse and the receiver phase.